The Astrophysical Journal Letters, 908:L52 (7pp), 2021 February 20 https://doi.org/10.3847/2041-8213/abe407

Kinetic Simulations of Electron Pre-energization by Magnetized Collisionless Shocks in Expanding Laboratory Plasmas

K. V. Lezhnin[1], W. Fox[1,2], D. B. Schaeffer[1], A. Spitkovsky[1], J. Matteucci[1], A. Bhattacharjee[1,2], and K. Germaschewski[3]
[1] Department of Astrophysical Sciences, Princeton University, Princeton, NJ 08544, USA; klezhnin@princeton.edu
[2] Princeton Plasma Physics Laboratory, Princeton University, Princeton, NJ 08543, USA
[3] Department of Physics and Space Science Center, University of New Hampshire, Durham, NH 03824, USA
Received 2020 December 1; revised 2021 February 5; accepted 2021 February 7; published 2021 February 25

Abstract

Collisionless shocks are common features in space and astrophysical systems where supersonic plasma flows interact, such as in the solar wind, the heliopause, and supernova remnants. Recent experimental capabilities and diagnostics allow detailed laboratory investigations of high-Mach-number shocks, which therefore can become a valuable way to understand shock dynamics in various astrophysical environments. Using 2D particle-in-cell simulations with a Coulomb binary collision operator, we demonstrate the mechanism for generation of energetic electrons and experimental requirements for detecting this process in the laboratory high-Mach-number collisionless shocks. We show through a parameter study that electron acceleration by magnetized collisionless shocks is feasible in laboratory experiments with laser-driven expanding plasmas.

Unified Astronomy Thesaurus concepts: Shocks (2086); Planetary bow shocks (1246); Laboratory astrophysics (2004); Plasma physics (2089)

Both Earth- and space-based detections of energetic particles spanning from MeV to EeV indicate that there are universal mechanisms for particle energization in astrophysical plasmas (Glasmacher et al. 1999). Two major plasma physics phenomena, magnetic reconnection (Yamada et al. 2010; Bulanov 2016) and collisionless shocks (Treumann 2009; Burgess & Scholer 2015), are usually considered as main contributors to energetic particle populations. Magnetized collisionless shocks are naturally formed in many space environments with a preexisting magnetic field, such as galaxy clusters, supernova remnants, and solar winds. The Fermi mechanism, commonly known as diffusive shock acceleration (DSA; Krymsky 1977; Bell 1978a, 1978b), is a mechanism by which shocks can energize particles, creating a power-law energy spectrum of charged particles due to scattering of energized particles back and forth between upstream and downstream.

One of the major questions of electron energization by high-Mach-number magnetized collisionless shocks is the so-called "injection problem": in order to enter the Fermi energization cycle, particles must be pre-energized from the thermal level to have a gyroradius large enough to be able to scatter on upstream and downstream waves. Based on simulations (e.g., Amano & Hoshino 2007, 2009, 2010; Guo et al. 2014), several different competing mechanisms have been proposed, but the need for a conclusive model still exists (Katou & Amano 2019). Besides that, energetic particles are observed in the shock transition layer of moderate-level Alfvén Mach number shocks with $M_A \sim 10$, even though turbulence in upstream and downstream may not be developed enough for lower shock speeds; thus, some mechanism other than DSA should be responsible for particle energization (Matsumoto et al. 2015). Moderate-level Alfvén Mach number shocks are observed in the Earth magnetosphere, and the presence of energized electrons was revealed from data by the Cassini satellite (Masters et al. 2013).

Laboratory astrophysics experiments using expanding ablation plasmas from high power laser-solid interactions provide a platform for modeling of astrophysical processes, such as magnetic reconnection (Nilson et al. 2006; Zhong et al. 2010; Dong et al. 2012; Rosenberg et al. 2015a, 2015b), collisionless shocks (Schaeffer et al. 2017a, 2017b, 2019; Umeda et al. 2019; Fiuza et al. 2020), and Weibel instability (Fox et al. 2013; Huntington et al. 2015), allowing for detailed diagnostics (Schaeffer et al. 2019) and controllable dimensionless parameters. Recently, magnetized collisionless shock formation with $M_A \sim 15$, and upstream electron beta $\beta_e = 2\mu_0 p_e/B^2 \sim 1$ was observed in the lab at the OMEGA laser facility (Schaeffer et al. 2017a, 2017b). Laboratory experiments with repeatable and controlled conditions and diagnostics, which span local and global plasma scales can provide important information for solving the shock acceleration problem, benchmarking simulation, and ultimately providing important insights into interpreting energized particle observations in space and astrophysical plasmas. Simulations using the Plasma Simulation Code (PSC; Germaschewski et al. 2016), which can match almost all dimensionless parameters of the system, allow detailed interpretation and predictions for the experiments. A significant opportunity is therefore to design experiments to measure the efficiency of particle acceleration by shocks, and study how it relates to the geometry, plasma and field parameters, and microphysics of the shock.

In this Letter, we demonstrate with simulations the possibility of, and requirements for, observing electron pre-energization in magnetized shocks in the laboratory. The preacceleration is attributed to shock drift acceleration (SDA), and we provide predictions for the first laboratory demonstration of this phenomenon. In contrast to typical shock simulations initiated by a moving simulation wall, we directly simulate a self-consistent shock formation created by a laser-driven piston in plasma, including Coulomb particle collisions (Fox et al. 2018), providing insights into the temporal behavior of particle acceleration in this strongly driven system. This leads to experimental requirements on the shock evolution time needed to distinguish particles accelerated at the shock from those generated by laser heating. Finally, we conduct

simulations for a range of Mach numbers, collisionalities, and magnetic field inclinations, and find the optimal values for obtaining rapid particle acceleration at parameters that are not too distant from parameters obtained in recent laser-driven shock experiments, and therefore may be possible in near future experiments.

We perform simulations using the particle-in-cell code PSC, which has a module to simulate binary collisions and a heating operator to mimic laser-foil interaction (Germaschewski et al. 2016; Fox et al. 2018). The 2D simulation grid is in the x–z plane, with z being the shock propagation and primary ablation direction. In the simulations, a high density target is heated, which produces an energetic ablation plume (the "piston") expanding from a high density reservoir at density $n_{\rm ab}$ and temperature $T_{\rm ab}$, which interacts with and drives a shock in a low density magnetized background plasma (the "upstream") at density $n_{\rm up}$, $T_{\rm up}$, with magnetic field $B_{\rm up}$ (Fox et al. 2018; Schaeffer et al. 2020).

For simulating shocks, it is most convenient to work in ion-scale units based on the plasma upstream conditions, where we measure density compared to upstream density $n_{\rm up}$, distance in units of $d_{\rm i,up}$, and time $\Omega_{\rm i}^{-1}$. Here, $d_{\rm i,up} \equiv c/\omega_{\rm pi,up}$ is the ion skin depth calculated at the upstream density $n_{\rm up}$ and $\Omega_{\rm i} \equiv eB_{\rm up}/m_{\rm i}$ is the ion upstream gyrofrequency. Matching these simulations to experiments based on ion-scale units is discussed in detail in Fox et al. (2018). The key to matching an experimental case is to match the dimensionless parameters $n_{\rm up}/n_{\rm ab}$ and $T_{\rm up}/T_{\rm ab}$, which gives the strength of the piston (which then controls the shock Mach number), and $\beta_{\rm e,up} = 2\mu_0 n_{\rm up} T_{\rm up}/B_{\rm up}^2$, which sets the upstream magnetization. In this work we simulate quasi-perpendicular shocks and therefore the initial magnetic field is oriented "out-of-plane," $\boldsymbol{B}_{\rm up} = B_{\rm up}(\sin\theta_{\rm Bn}\boldsymbol{e_y} + \cos\theta_{\rm Bn}\boldsymbol{e_z})$, with inclination angle $\theta_{\rm Bn}$ ranging from 50° to 90°. The simulation box is $10 \times 400\, d_{\rm i,up}$ in the x–z plane. The runs are performed with upstream plasma beta $\beta_{\rm e,up} = 2$ with upstream density $n_{\rm up}/n_{\rm ab} = 0.05$ and upstream temperature $T_{\rm i,up} = T_{\rm e,up} = 0.002 m_e c^2$. We conduct both collisionless and modestly collisional runs, where the collisionality is parameterized by $\Lambda_{\rm up} \equiv \lambda^{\rm th}_{\rm e,mfp}/d_{\rm i,up} \approx 0.01 - 0.34$, where $\lambda^{\rm th}_{\rm e,mfp}$ is the mean free path calculated for an electron traveling in upstream plasma with $T_{\rm up}$ and $n_{\rm up}$. The shock speed is $M_{\rm A} = v_{\rm sh}/V_{\rm A,up} \approx 15$ and $M_{\rm e}^{\rm th} = v_{\rm sh}/v_{\rm e,up}^{\rm th} \approx 1.1$, where $v_{\rm e,up}^{\rm th} = \sqrt{2T_{\rm e,up}/m_{\rm e}}$ is the upstream electron thermal speed. We conduct simulations for $6\Omega_{\rm i}^{-1}$, which is sufficient to observe formation of the self-consistent shock structure with a developed downstream (Schaeffer et al. 2020) and the initial stages of particle acceleration.

We note the following numerical details of running these simulations using the particle-in-cell technique. The total number of particles per cell is chosen to be 500 at ablation density $n_{\rm ab}$. The simulation box is 600 cells in x and 24000 cells in z, corresponding to a resolution of six grid nodes per $d_{\rm e,up}$, where $d_{\rm e,up} = c/\omega_{\rm pe,up}$ is the electron skin depth calculated at the upstream density $n_{\rm up}$. The heating operator is uniform in the transverse direction and applied during the first $2\,\Omega_{\rm i}^{-1}$. The simulations were carried out with a reduced ion-to-electron mass ratio $m_{\rm i}/m_{\rm e} = 100$ (meaning $d_{\rm i} = 10 d_{\rm e}$) and a reduced speed of light compared to the electron thermal speed, $T_{\rm e,ab}/m_{\rm e}c^2 = 0.04$ (Fox et al. 2018). A single ion species plasma with $Z = 1$ is considered. We also tag particles that originated from the ablating foil ("piston" particles) and from the ambient magnetized plasma ("background" particles) in order to clarify the physics of piston-driven collisionless shocks.

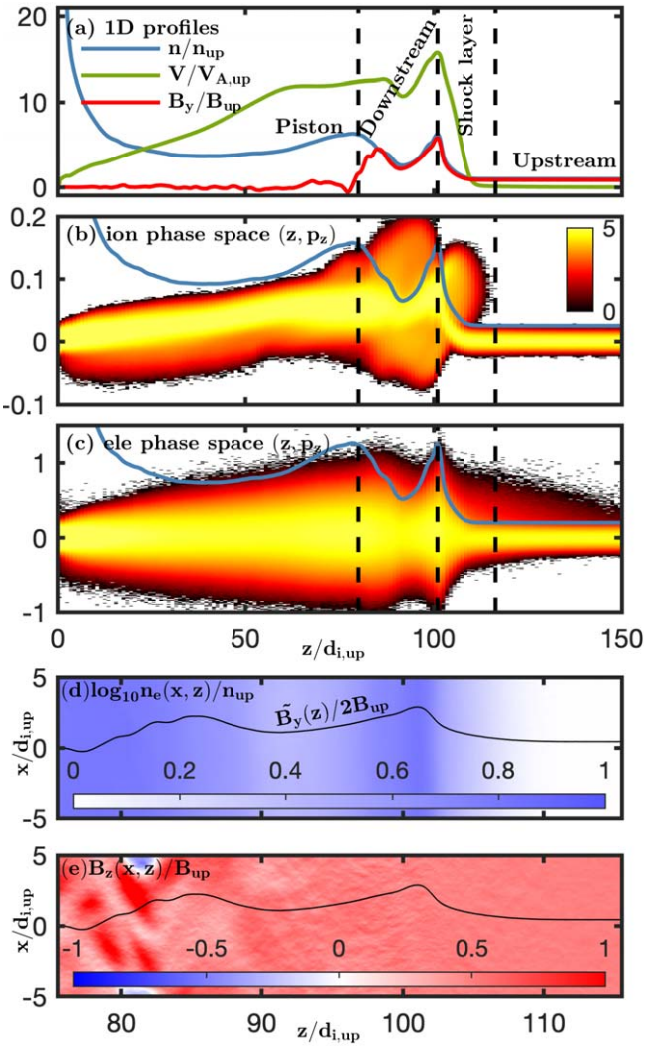

Figure 1. Structure of an ablation driven shock, which self-consistently accelerates a fast electron population at $\Omega_i t = 6$. $M_{\rm A} \approx 15$, $\beta_{\rm e,up} = 2$, $\theta_{\rm Bn} = 60°$, $m_{\rm i}/m_{\rm e} = 100$, and $\Lambda_{\rm up} = 0.34$. Transversely averaged 1D profiles of plasma density, B_y, and flow speed (a), ion (b), and electron (c) z–p_z phase distributions and ion density profiles. Dashed vertical lines separate shock regions—piston, downstream, shock layer, and upstream. 2D profiles of (d) $\log_{10} n_{\rm e}/n_{\rm up}$ and (e) $B_z/B_{\rm up}$ for $z/d_{\rm i,up} = 75 - 115$.

Figure 1(a) shows transversely averaged 1D profiles at $\Omega_i t = 6$ for a simulation with $M_{\rm A} \approx 15$, $\beta_{\rm e,up} = 2$, $M_{\rm e}^{\rm th} \approx 1.1$, $\theta_{\rm Bn} = 60°$, and $\Lambda_{\rm up} = 0.34$, which exhibits electron preacceleration. This shock is self-consistently formed by a piston plasma expanding into the ambient magnetized plasma and requires a few ion gyrotimes to separate from the piston. Here, we define the shock regions as follows. The piston is defined as the region from the target ($z = 0$) to the edge of the magnetic cavity ($z/d_{\rm i,up} = 80$); the shock layer is defined as the region between the overshoot peak ($z/d_{\rm i,up} = 101$) and the location where ion gyration stops ($z_{\rm up}/d_{\rm i,up} \equiv (z_{\rm shock} + \rho_i)/d_{\rm i,up} = 114$); the downstream and upstream appear to the left and to the right from the shock layer. Here, $\rho_i \approx 13 d_{\rm i,up}$ is the ion gyroradius at the shock front. The jump ratios for magnetic field, density, and electron and ion temperatures are $B_{\rm down}/B_{\rm up} \approx 4$, $n_{\rm i,down}/n_{\rm i,up} \approx 3.7$, $T_{\rm e,down}/T_{\rm e,up} \approx 18.4$, and $T_{\rm i,down}/T_{\rm i,up} \approx 38.8$, which is in approximate agreement with the Rankine–Hugoniot

MHD jump conditions in the $M_A \gg 1$ limit (Fitzpatrick 2014), and which indicate the formation of a shock. Recently, Schaeffer et al. (2020) showed that after $\approx 5\ \Omega_i^{-1}$ the piston-driven shock may be considered as a self-consistent shock structure with the developed downstream and without any influence from the piston on the subsequent shock evolution. Figure 1(b) shows the ion z–p_z phase space distribution, with the blue line representing the ion density profile. Here we observe ion reflection in the shock layer near $z \approx 107.5 d_{i,up}$. In this quasi-perpendicular shock with $\theta_{Bn} = 60°$, ions are not reflected far upstream, gyrating with $\rho_i = M_A\, d_{i,shock} \approx 13\, d_{i,up}$.

Electron energization in the shock layer and upstream is also observed in the electron z–p_z phase space distribution, Figure 1(c), around $z/d_{i,up} \approx 100$–130. These fast particles have significantly enhanced momentum and $\sim 100\times$ energy compared to the thermal upstream particles, and may ultimately start the cyclic DSA process (Xu et al. 2020). A similar effect was observed in prior 1D/2D PIC simulations (Amano & Hoshino 2007, 2009; Guo et al. 2014) with shock parameters close to those presented in this work and was interpreted as a combination of shock surfing acceleration (SSA), in which electrons are preaccelerated by electrostatic solitary waves formed in the shock foot region by multistream instabilities, and SDA, in which electrons are reflected by the shock magnetic overshoot (Treumann 2009).

We find that collisions play an important role, both in terms of establishing the shock structure and then in terms of modifying the electron pre-energization. At moderate collisionality, as for the present simulation with $\Lambda_{up} = 0.34$, collisions reduce fluctuations in the shock layer in comparison to analogous collisionless runs, but do not completely damp particle acceleration. Figures 1(d) and (e) show 2D density distribution and 2D distribution of z-component of the magnetic field, respectively. By this time in the simulation, no prominent structure in density or magnetic fields is seen, with only minor corrugations found in the piston-downstream contact layer ($z/d_{i,up} \approx 80$). As the collisionality is further increased, the preacceleration can indeed be destroyed by collisions, and this is discussed in detail below.

Figure 2 shows in greater detail the time history of electron acceleration. Figures 2(a) and (b) show the electron phase space for piston- and background-tagged electrons at $\Omega_i t = 6$, respectively. The same shock structure regions as above are specified here with dashed lines. Blue curves indicate the total electron density profiles, while the green lines indicate the piston electron (Figure 2(a)) or background electron (Figure 2(b)) density profiles. Due to collisions, the piston electrons are slowed in the ambient plasma and are largely stopped before the shock, completely vanishing from the upstream at later stages of the shock evolution. Figures 2(a) and (b) show that the whole shock structure (downstream, shock layer, and upstream) is well developed and independent of the piston at this time.

Figure 2(c) shows the energy spectrum in the upstream (from z_{up} to the right boundary of the simulation box) at several times from $\Omega_i t = 0$ to 6. The contribution to the spectrum from piston-tagged particles is shown with dashed lines. The fit of the bulk part of the late-time electron spectrum is also presented (green solid-circled line). Here, we see that at $t = 2\ \Omega_i^{-1}$ (the duration of the experiment in Schaeffer et al. 2017a, 2017b), the nonthermal tail is already there, though the downstream is not yet developed at that time and the

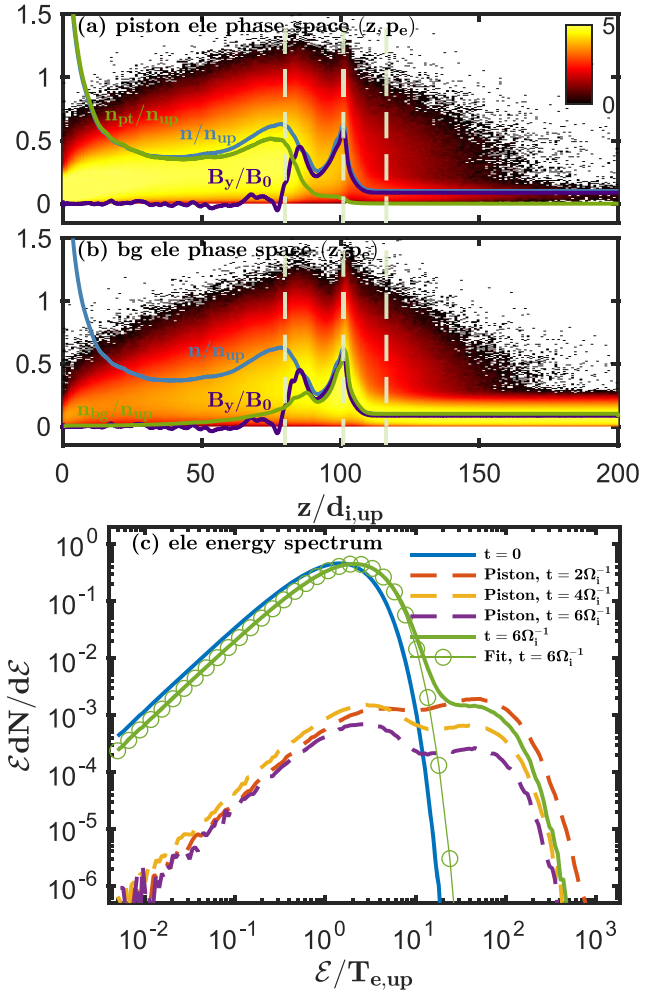

Figure 2. z–$p_{e,z}$ phase space distribution for particles tagged as (a) piston and (b) background electrons; (c) upstream electron energy spectrum for the same run as in Figure 1. Dashed lines in (c) show the piston-tagged particle energy spectrum in the upstream at $t = 2$, 4, 6 Ω_i^{-1}, and the circled line is the fit of the bulk part of the upstream spectrum at 6 Ω_i^{-1}.

nonthermal population is predominantly comprised of piston particles. We find that it requires at least 6 Ω_i^{-1} for the nonthermal tail to be dominated by background particles. The dashed magenta line, representing the energy spectrum of piston-tagged electrons at $t = 6\ \Omega_i^{-1}$ in Figure 2(c), shows that by this time the piston contribution to the energized particles is small in comparison to the background particles, comprising $<10\%$ for $\mathcal{E}/T_{e,up}$ in the range of 10–100. Electron energization is fairly efficient: the fraction of upstream electrons with energy $\mathcal{E} > 20\ T_{e,up}$ is $\epsilon_e \sim 5\%$, in agreement with 1D simulations with similar dimensionless shock parameters (Xu et al. 2020). We convert maximum electron energy to physical units, assuming that it is proportional to the kinetic energy of the shock flow relative to the upstream, $\mathcal{E}_{e,max} \propto m_i v_{sh}^2$. Auxiliary simulations with two-slab shock geometry verify this scaling. For $v_{sh} = 700\ \mathrm{km\ s^{-1}}$ (typical laboratory speeds), $\mathcal{E}_{e,max} \approx 11$ keV.

Figure 3 illustrates the mechanism for electron energization for an electron that ends up in the upstream. Figure 3(a) shows the evolution of the density profile over time superposed with a particle trajectory near the shock. It shows the evolution of the shock structure (dashed line labeled "shock"), expansion of the ablating foil (white area labeled "expanding foil"), propagation of the piston (yellow area labeled "piston"), and development of the

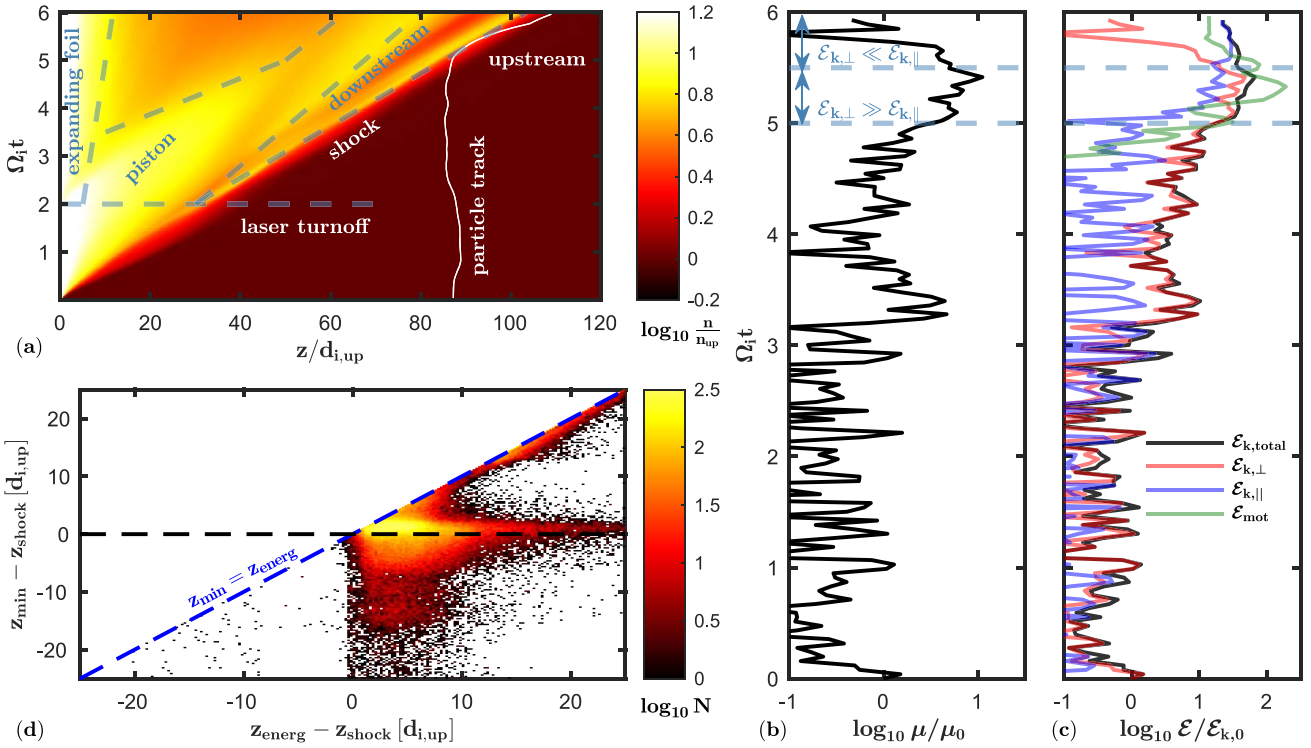

Figure 3. Trajectory of the energized electron (white line) in (a) density profile evolution over time; (b) first adiabatic invariant normalized to its initial value; and (c) total kinetic energy (black), perpendicular kinetic energy (red), parallel kinetic energy (blue), and energy deposited onto a particle by motional electric field (green) evolution of a particle normalized to initial electron energy. (d) 2D histogram of energized ($p_e/m_e c > 0.3$) particles reflected into the upstream ($z > z_{up}$) at the end of simulation in ($z_{energ} - z_{shock}$, $z_{min} - z_{shock}$) coordinates. The blue dashed line demarkates $z_{min} <= z_{energ}$, which is required by definition.

contact discontinuity and shock downstream (starting from $\sim 3\,\Omega_i^{-1}$). The white line shows a particle track in (z, t) space. During the first $5\,\Omega_i^{-1}$, the electron quivers around $z/d_{i,up} \approx 87$ with nearly constant magnetic moment $\mu \equiv v_{e\perp}^2/B$ (Figure 3(b)) and energy (Figure 3(c)), and once the electron gets within $\sim 1-10\,d_{i,up}$ from the overshoot, the electron experiences a nonadiabatic (Figure 3(b)) gain of perpendicular energy over a time $\sim \Omega_i^{-1}$. This type of particle energization is consistent with SDA (Guo et al. 2014), which only requires (a) the presence of the motional electric field being dominantly responsible for perpendicular energy gain (Figures 3(c)) and (b) ∇B drift in the shock layer ($\nabla B \times \boldsymbol{B} \cdot \hat{x} \neq 0$, as seen in Figure 1(a)). After traveling with the shock front for $\approx 0.5\,\Omega_i^{-1}$ at a location within a few $d_{i,up}$ from the overshoot, the accelerated electron is reflected from the magnetic overshoot to the upstream, losing its perpendicular energy (Figure 3(c)) and escaping along the magnetic field line. Tracking back all energized particles in the upstream (i.e., particles with $p_e/m_e c > 0.3$ and $z > z_{up}$), we estimate where this particle population was accelerated (i.e., where $p_e/m_e c > 0.3$ for the first time throughout the simulation) with respect to the shock, $z_{energ} - z_{shock}$, and how deep these particles get into the shock over the whole shock evolution, $z_{min} - z_{shock}$, Figure 3(d). This analysis indicates that particles are predominantly energized in the shock foot ($z_{energ} - z_{shock} > 0$), rather than in the downstream, and that only a small number of particles even sample the downstream. Average values of these quantities are $\langle z_{energ} - z_{shock} \rangle \approx 6.3 d_{i,up}$ and $\langle z_{min} - z_{shock} \rangle \approx 1.1 d_{i,up}$. The mean energy e-folding time of this population is $1.8\,\Omega_i^{-1}$, which is again in good agreement with Guo et al. (2014). The typical energy gain in SDA, $\Delta\mathcal{E}_{SDA}/T_{e,up} = M_A^{-1}(m_i/m_e)(m_e v_{sh}^2/T_{e,up}) \sin\theta_{Bn}(\delta x/d_{i,up}) \sim 127$ ($\Delta\mathcal{E}_{SDA}/m_e c^2 \sim 0.3$), is fairly consistent with energy gains observed in our simulations ($\delta x \sim 10 d_{i,up}$ is the transverse distance traveled by a electron in the shock layer before the reflection). SSA (Amano & Hoshino 2007) and cyclic SDA (Guo et al. 2014) were not observed in the run, since the waves are suppressed in collisional simulations: $\delta B/B_{up} < 20\%$ and $E_{es}/B_{up} < 0.1$ in the collisional case, in contrast to $\delta B/B_{up} \sim 100\%$ and $E_{es}/B_{up} \sim 0.3$ in the analogous collisionless run. Here, δB is the magnetic field perturbation magnitude and E_{es} is the electrostatic component of the electric field.

Figures 4(a) and (b) summarize a set of our simulations with $M_A \approx 15$, $\beta_{e,up} = 2$, and $\Lambda_{up} = 0.34$ where we have varied the shock angle θ_{Bn}. In this scan, we used a transverse size of the box equal to $2 d_{i,up}$ since in our case the role of transverse structure of the shock was found to be insignificant for electron acceleration. We also varied the collisionality (Λ_{up}) and Alfvén Mach number M_A, and observe significant energization of the upstream electron population. We quantify the accelerated electrons in terms of two parameters: $\overline{\mathcal{E}_{e,up}} \equiv \int_{z_{up}} \mathcal{E} f(\mathcal{E}) d\mathcal{E} \Big/ \int_{z_{up}} f(\mathcal{E}) d\mathcal{E}$, which is the energy moment of the distribution function $f(\mathcal{E})$ calculated in the upstream; and shock reflectivity R, which is the fraction of nonthermal particles in the upstream $R \equiv n_{e,up}(\mathcal{E} > 20\,T_{e,up})/n_{e,up}$. Error bars are obtained by varying the analysis window within $5 d_{i,up}$. The green asterisk corresponds to the reference simulation described above. A parametric scan shows a range around $R \approx 1\%$–2% of nonthermal particles and $\overline{\mathcal{E}_{e,up}}/T_{e,up} \approx 3$ for $\theta_{Bn} = 60°$. The trend toward a smaller number of particles for larger shock angles is in qualitative agreement with similar simulations in Amano & Hoshino (2007). This is tied to the size of the loss cone allowing particles to escape along the magnetic field line when the condition $u_\perp \geqslant C_{s,up}(B_{up}/B_{overshoot})^{1/2}$ is satisfied (Amano &

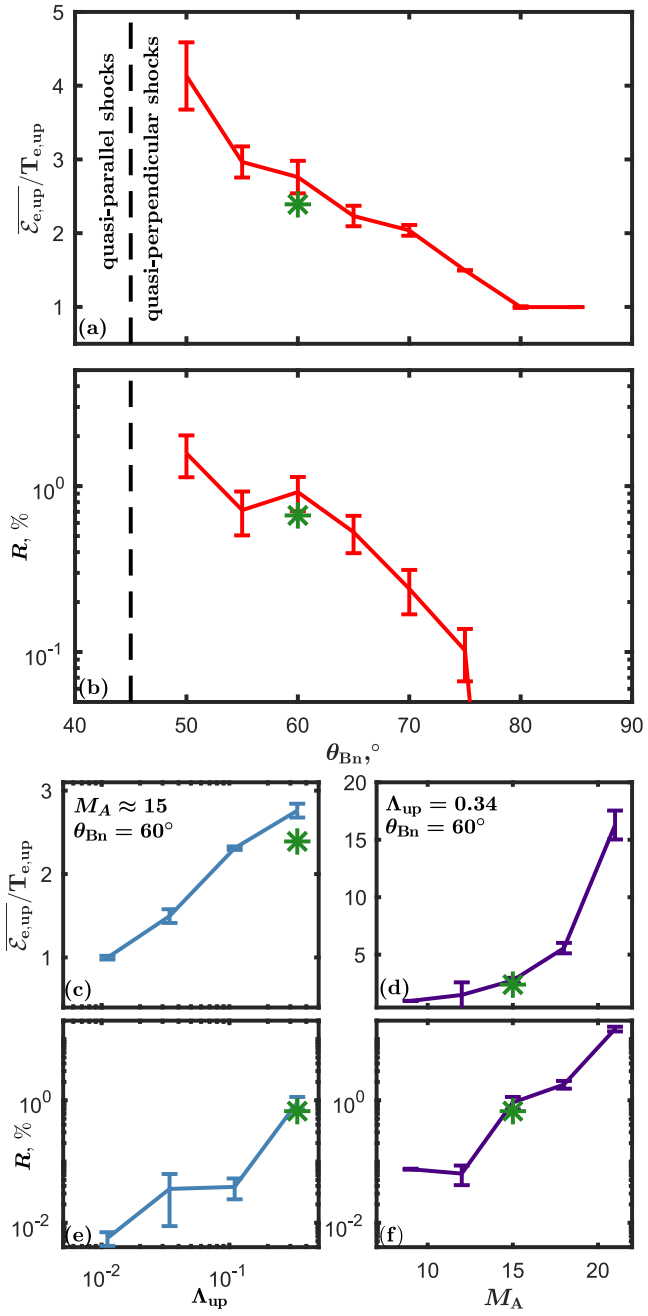

Figure 4. Dependence of the properties of the nonthermal electron population —(a) $\overline{\mathcal{E}_{e,up}}/T_{e,up}$ and (b) R—on shock angle θ_{Bn} for simulations with $M_A \approx 15$, $\Lambda_{up} = 0.34$, and transverse box size of $2d_{i,up}$; scans on (c), (e) Λ_{up} and (d), (f) M_A for simulations with $\theta_{Bn} = 60°$. Green asterisk corresponds to the reference simulation described in Figures 1–3.

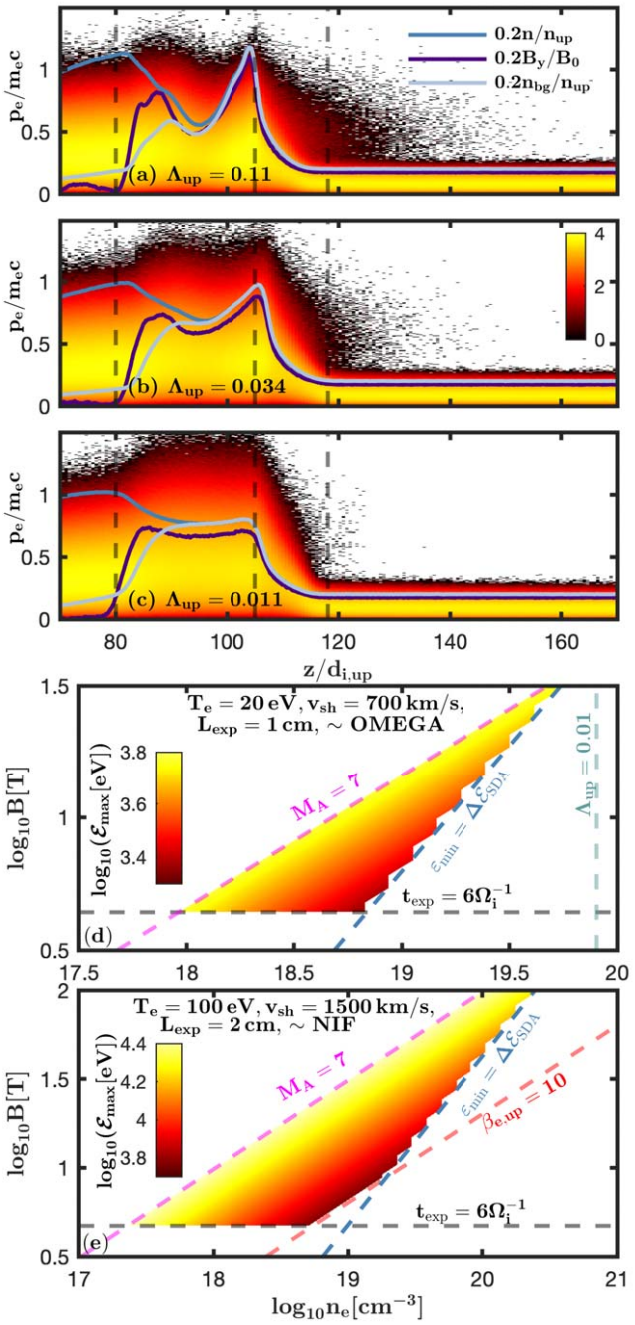

Figure 5. Electron phase space distribution in $(z/d_{i,up}, p_e/m_ec)$ coordinates for the parameters of the run presented above with the collisionality level Λ_{up} being (a) 0.11, (b) 0.034, and (c) 0.011. The gradual drop of the maximum energies and preaccelerated electron numbers is seen for larger collisionalities. Colormap of the maximum electron energy achievable by collisionless shock via SDA that may be detected in the experimental setup simular to (d) OMEGA and (e) NIF.

Hoshino 2007). Here, $u_\perp$ is the perpendicular velocity with respect to local magnetic field and $C_{s,up}$ is the upstream sound speed. The fraction of nonthermal particles saturates for angles smaller than 60°, which is again in agreement with the analytical prediction from Amano & Hoshino (2007). Figures 4(c)–(f) demonstrate a scan on collisionality (Figures 4(c) and (e)) and M_A (Figures 4(d) and (f)). They show the robustness of the proposed preacceleration mechanism to variations in shock speed for Alfvén Mach numbers larger than threshold for injection M_A^{inj}, $M_A \geqslant M_A^{inj} \equiv 0.5\cos(\theta_{Bn})\ (\beta_{e,up}\, m_i/m_e)^{1/2} \approx 3.5$ (Amano & Hoshino 2010). Figures 5(a)–(c) present the collisionality scan for Λ_{up} from 0.11 to 0.011, and it clearly shows how the gradual transition to more collisional plasma suppresses the population of energetic electrons in the upstream. The collisionality threshold criteria is found to be $\Lambda_{up} \gg 0.01$.

Let us summarize the experimental requirements that will allow us to study shock acceleration of electrons. (1) Shock

parameters—we need the shock parameters to be in the right regime for the efficient SDA manifestation, which, according to our simulations and data from literature, requires $M_A \geqslant 7 \geqslant M_{inj}$ and $\beta_{e,up} \sim 1$. The shock angle is also important, as only quasi-perpendicular shocks with $\theta_{Bn} < 70^\circ$ show significant acceleration. (2) System size—we require the spatial size of the setup to be large enough, so the shock will have enough time to develop and accelerate electrons. This is a constraint on both the experiment time t_{exp} and system size L_{exp}, which are related by $t_{exp} = L_{exp}/v_{sh}$, where v_{sh} is the shock speed. We find that the shock develops in $\approx 2\Omega_i^{-1}$, that the timescale for particle acceleration is $\approx 1.8\Omega_i^{-1}$. However, we then find $\approx 6\Omega_i^{-1}$ are required for the background-accelerated particles to dominate, allowing a clean detection of acceleration. (3) Collisionality—another condition for the experimental observation of nonthermal electrons is sufficiently low collisionality. This requirement can be naturally separated into two subcategories: (I) sufficiently low collisionality for the SDA to effectively accelerate electrons (our numerical analysis implies that the sufficient condition is $\Lambda_{up} \gg 0.01$) and (II) sufficiently low collisionality for the accelerated electrons to leave the shock layer and reach the detector without significant energy losses, i.e., the mean free path of the energetic electron is larger than the system size ($\lambda^{\varepsilon}_{e,mfp}/L_{exp} \geqslant 1$). Another condition that is related to collisionality is that $\mathcal{E}_{max}$, the maximum electron energy that can be achieved by the given collisionless shock via SDA (Guo et al. 2014), is no less than the minimum electron energy that satisfies escape conditions, ε_{min}: $\mathcal{E}_{max} \geqslant \varepsilon_{min}$.

Figures 5(d) and (e) illustrate the parameter space (n, B, $\mathcal{E}_{max}$) which satisfies the conditions listed above for typical parameters of experimental setups at large laser facilities like OMEGA and NIF. For typical experimental parameters at the OMEGA facility (system size $L_{exp} = 1$ cm, background plasma temperature $T_e \sim 20$ eV, shock speed $v_{sh} = 700\,\mathrm{km\,s^{-1}}$; Schaeffer et al. 2017a, 2017b), observation of nonthermal electrons requires a regime with $B \sim 10$ T magnetic field and upstream plasma density $n_e \sim 10^{18}$–$10^{19}\,\mathrm{cm^{-3}}$. In this case, we expect the electrons of energies between $\varepsilon_{min} = 1.5$ keV and $\mathcal{E}_{max} = 5$ keV to escape the experimental setup and be available for observation. These parameters are already available at the OMEGA facility (e.g., magnetic fields of around 15 T were previously reported in Fiksel et al. 2015). For NIF-like parameters ($L_{exp} = 2$ cm, $T_e = 100$ eV, $v_{sh} = 1500\,\mathrm{km\,s^{-1}}$), a regime with $B \sim 10^1$ T and $n_e \sim 10^{18}$–$10^{19}\,\mathrm{cm^{-3}}$ is needed, allowing observations of particles in the range from 1.5 to 10 keV; our PIC simulations demonstrate that such high electron energies are achievable. While magnetized collisionless shock experiments have not yet been conducted at NIF, these values are reasonable extensions from OMEGA experiments to a larger laser facility like NIF. Some parameters, such as temperature and flow speed, were recently reported for the experimental study of a Weibel shock at NIF (Fiuza et al. 2020).

It is useful to note that we do not expect a significant influence of the shock curvature on the SDA acceleration of electrons. In principle, the shock front curvature does affect the efficiency of the SDA, since it requires a significant transverse motion of the preaccelerated particle. But, in our case, at later stages of shock evolution, the radius of curvature scales as $M_A\Omega_i t$ and, after a few ion gyrotimes, will be significantly larger than transverse acceleration scales within the shock. Thus, the SDA mechanism will not be affected.

It is also important to note that we conduct 2D simulations with "out-of-plane" magnetic field (i.e., with a significant magnetic field component along $\boldsymbol{e_y}$, which is perpendicular to the simulation box plane $\{\boldsymbol{e_x}, \boldsymbol{e_z}\}$), which is known to affect the structure of the shock itself (Wieland et al. 2016; Bohdan et al. 2017), as well as the electron energization efficiency (Guo et al. 2014; Crumley et al. 2019; Xu et al. 2020). In Bohdan et al. (2017), it was shown that simulations with strictly out-of-plane magnetic field yield an order of magnitude larger preaccelerated electron fraction in comparison to in-plane runs, since the former is more suitable for capturing Buneman modes (which are not developed in case of our shock parameters as explained above). Our auxiliary 2D in-plane magnetic field simulation with $M_A \approx 15$, $\beta_{e,up} = 2$, $\Lambda_{up} = 0.34$, and $\theta_{Bn} = 60^\circ$ suggests that in-plane runs demonstrate a suppressed electron energization efficiency in comparison to out-of-plane runs, giving $R \approx 0.1\%$ and $\overline{\mathcal{E}_{e,up}}/T_{e,up} \approx 1.5$. This may be attributed to a significantly more laminar structure of motional electric field in the out-of-plane case, which overperforms the in-plane case despite higher jump ratio and shock speed (Crumley et al. 2019). The differences between in-plane and out-of-plane 2D results call for 3D simulations. These are very challenging to run under relevant system sizes and parameters and therefore are at a relatively earlier stage of study. Nevertheless we note a few recent studies that bear on our results. Xu et al. (2020) showed that 3D simulations of moderate M_A quasi-perpendicular shocks lead to approximately an order of magnitude decrease in electron reflectivity in comparison to identical 1D runs. Second, most recently R. Xu et al. (2021, in preparation) addressed the question of electron reflectivity from quasi-perpendicular shocks in out-of-plane 2D, in-plane 2D, and 3D geometry. They find that electron reflection efficiency in 3D is slightly smaller than in out-of-plane 2D geometry, but much larger than in the in-plane 2D case for identical shock parameters. These results suggest that our out-of-plane 2D simulations are a good estimate of realistic electron reflectivity in three dimensions. In order to study the convergence of our results, we compared our runs with $M_A \approx 15$, $\beta_{e,up} = 2$, $\Lambda_{up} = 0.34$, $\theta_{Bn} = 60^\circ$, and varying transverse size (strictly 1D, $6d_{e,up}$, $20d_{e,up}$, and $100d_{e,up}$), mass ratio (running a strictly 1D run with $m_i/m_e = 400$), and absolute value of the shock speed relative to the speed of light, and concluded that changing these parameters does not significantly affect R and $\overline{\mathcal{E}_{e,up}}$. Thus, we conclude that a sufficient level of electron energization is expected to be found in the shock upstream for a realistic mass ratio and 3D geometry case.

In summary, we have conducted a multiparameter investigation of electron preacceleration by collisionless magnetized shocks in experimental conditions of expanding laboratory laser plasmas. Our 2D PIC simulations show that it is possible to generate a population of nonthermal electrons in the upstream and shock layer with energies up to tens of keV when the shock parameters are close to those that were obtained experimentally in Schaeffer et al. (2017a, 2017b, 2019). We also formulate the experimental conditions needed for the robust observation of electron injection by magnetized collisionless shocks. In the near future, we believe controlled laboratory experiments on electron energization by magnetized collisionless shocks will allow for better understanding of electron energization by moderate-level Alfvén Mach number shocks observed in the Earth's magnetosphere, as

well as to address the injection problem for high-Mach-number shocks.

Simulations were conducted on the Titan and Summit supercomputers at the Oak Ridge Leadership Computing Facility at the Oak Ridge National Laboratory, supported by the Office of Science of the DOE under Contract No. DE-AC05-00OR22725. This research was also supported by the DOE under Contracts No. DE-SC0014405, DE-SC0016249, and DE-NA0003612, and NSF grants PHY-1748958, AST-1814708, PHY-1804048, and NASA under Grant No. 80NSSC19K0493.

ORCID iDs

K. V. Lezhnin https://orcid.org/0000-0002-7636-069X

References

Amano, T., & Hoshino, M. 2007, ApJ, 661, 190
Amano, T., & Hoshino, M. 2009, ApJ, 690, 244
Amano, T., & Hoshino, M. 2010, PhRvL, 104, 181102
Bell, A. R. 1978a, MNRAS, 182, 147
Bell, A. R. 1978b, MNRAS, 182, 443
Bohdan, A., Niemiec, J., Kobzar, O., & Pohl, M. 2017, ApJ, 847, 71
Bulanov, S. V. 2016, PPCF, 59, 014029
Burgess, D., & Scholer, M. 2015, Collisionless Shocks in Space Plasmas (Cambridge: Cambridge Univ. Press)
Crumley, P., Caprioli, D., Markoff, S., & Spitkovsky, A. 2019, MNRAS, 485, 5105
Dong, Q. L., Wang, S. J., Lu, Q. M., et al. 2012, PhRvL, 108, 215001
Fiksel, G., Agliata, A., Barnak, D., et al. 2015, RScI, 86, 016105
Fitzpatrick, R. 2014, Plasma Physics. An Introduction (Boca Raton, FL: CRC Press)
Fiuza, F., Swadling, G. F., Grassi, A., et al. 2020, NatPh, 16, 916
Fox, W., Fiksel, G., Bhattacharjee, A., et al. 2013, PhRvL, 111, 225002
Fox, W., Matteucci, J., Moissard, C., et al. 2018, PhPl, 25, 102106
Germaschewski, K., Fox, W., Abbott, S., et al. 2016, JCoPh, 318, 305
Glasmacher, M. A. K., Catanese, M. A., Chantell, M. C., et al. 1999, APh, 10, 291
Guo, X., Sironi, L., & Narayan, R. 2014, ApJ, 794, 153
Huntington, C. M., Fiuza, F., Ross, J. S., et al. 2015, NatPh, 11, 173
Katou, T., & Amano, T. 2019, ApJ, 874, 119
Krymsky, G. F. 1977, ASR USSR, 234, 1306
Masters, A., Stawarz, L., Fujimoto, M., et al. 2013, NatPh, 9, 164
Matsumoto, Y., Amano, T., Kato, T. N., & Hoshino, M. 2015, Sci, 347, 974
Nilson, P. M., Willingale, L., Kaluza, M. C., et al. 2006, PhRvL, 97, 255001
Rosenberg, M. J., Li, C. K., Fox, W., et al. 2015a, PhRvL, 114, 205004
Rosenberg, M. J., Li, C. K., Fox, W., et al. 2015b, NatCo, 6, 6190
Schaeffer, D. B., Fox, W., Follett, R. K., et al. 2019, PhRvL, 122, 245001
Schaeffer, D. B., Fox, W., Haberberger, D., et al. 2017a, PhRvL, 119, 025001
Schaeffer, D. B., Fox, W., Haberberger, D., et al. 2017b, PhPl, 24, 122702
Schaeffer, D. B., Fox, W., Matteucci, J., et al. 2020, PhPl, 27, 042901
Treumann, R. A. 2009, A&ARv, 17, 409
Umeda, T., Yamazaki, R., Ohira, Y., et al. 2019, PhPl, 26, 032303
Wieland, V., Pohl, M., Niemiec, J., Rafighi, I., & Nishikawa, K.-I. 2016, ApJ, 820, 62
Xu, R., Spitkovsky, A., & Caprioli, D. 2020, ApJL, 897, L41
Yamada, M., Kulsrud, R., & Ji, H. 2010, RvMP, 82, 603
Zhong, J., Li, Y., Wang, X., et al. 2010, NatPh, 6, 984